
Neural varifolds: an aggregate representation for quantifying the geometry of point clouds

Juheon Lee^{1*}, Xiaohao Cai², Carola-Bibian Schönlieb³, Simon Masnou⁴

¹ Independent Researcher

² School of Electronics and Computer Science, University of Southampton

³ Department of Applied Mathematics and Theoretical Physics, University of Cambridge

⁴ Institut Camille Jordan, Université Claude Bernard Lyon 1

Abstract

Point clouds are popular 3D representations for real-life objects (such as in LiDAR and Kinect) due to their detailed and compact representation of surface-based geometry. Recent approaches characterise the geometry of point clouds by bringing deep learning based techniques together with geometric fidelity metrics such as optimal transportation costs (e.g., Chamfer and Wasserstein metrics). In this paper, we propose a new surface geometry characterisation within this realm, namely a neural varifold representation of point clouds. Here the surface is represented as a measure/distribution over both point positions and tangent spaces of point clouds. The varifold representation quantifies not only the surface geometry of point clouds through the manifold-based discrimination, but also subtle geometric consistencies on the surface due to the combined product space. This study proposes neural varifold algorithms to compute the varifold norm between two point clouds using neural networks on point clouds and their neural tangent kernel representations. The proposed neural varifold is evaluated on three different sought-after tasks – shape matching, few-shot shape classification and shape reconstruction. Detailed evaluation and comparison to the state-of-the-art methods demonstrate that the proposed versatile neural varifold is superior in shape matching and few-shot shape classification, and is competitive for shape reconstruction.

1 Introduction

Point clouds are preferred in more and more applications including computer graphics, autonomous driving, robotics and augmented reality. However, manipulating/editing point clouds data in its raw form is rather cumbersome. Neural networks have made breakthroughs in a wide variety of fields ranging from natural language processing to computer vision. Point cloud data in general lack underlying grid structures. As a result, convolution operations on point cloud data require special techniques including voxelisation [1, 2, 3], graph representations [4, 5, 6] or point-wise convolutions [7, 8, 9]. Geometric deep learning and its variants have addressed technical problems of translating neural networks on point cloud data [5]. With advanced graph theory and harmonic analysis, convolutions on point cloud data can be defined in the context of spectral [4, 10] or spatial [11, 6] domains. Although geometric deep learning on point clouds has successfully achieved top performance in shape classification and segmentation tasks, capturing subtle changes in 3D surface remains challenging due to the unstructured and non-smooth nature of point clouds. A possible direction to learn subtle changes on 3D surface adopts some concepts developed in the field of theoretical geometric analysis. In other words, deep learning architectures might be improved by incorporating theoretical knowledge from geometric analysis. In this work, we introduce concepts

*This research is my personal endeavor and is unrelated to my current job.

borrowed from geometric measure theory, where representing shapes as measures or distributions has been instrumental.

Geometric measure theory has been actively investigated by mathematicians; however, its technicality may have hindered its popularity and its use in many applications. Geometric measure-theoretic concepts have recently been introduced to measure shape correspondence in non-rigid shape matching [12, 13, 14] and curvature estimation [15, 16]. We introduce the theory of varifolds to improve learning representation of 3D point clouds. An oriented d -varifold is a measure over point positions and oriented tangent k -planes, i.e., a measure on the Cartesian product space of \mathbb{R}^n and the oriented Grassmannian manifold $\tilde{G}(d, n)$. Varifolds can be viewed as generalisations of d -dimensional smooth shapes in Euclidean space \mathbb{R}^n . The varifold structure not only helps to better differentiate the macro-geometry of the surface through the manifold-based discrimination, but also the subtle singularities in the surface due to the combined product space. Varifolds provide representations of general surfaces without parameterization. They not only can represent consistently point clouds that approximate surfaces in 3D, but are also scalable to arbitrary surface discretisation (e.g., meshes). In this study, we use varifolds to analyse and quantify the geometry of point clouds.

Our contributions:

- Introduce the notion of neural varifold as a learning representation of point clouds. Varifold representation of 3D point clouds coupling space position and tangent planes can provide both theoretical and practical analyses of the surface geometry.
- Propose two algorithms to compute the varifold norm between two point clouds using neural networks on point clouds and their neural tangent kernel representations. The reproducing kernel Hilbert space of the varifold is computed by the product of two neural tangent kernels of positional and Grassmannian features of point clouds. The neural varifold can take advantage of the expressive power of neural networks as well as the varifold representation of point clouds.
- Apply the usage of neural varifold in evaluating shape similarity between point clouds on various tasks including shape matching, few-shot shape classification and shape reconstruction.

2 Related works

Geometric deep learning on point clouds. PointNet is the first pioneering work on point clouds. It consists of a set of fully connected layers followed by symmetric functions to aggregate feature representations. In other words, PointNet is neural networks on a graph without edge connections. In order to incorporate local neighbourhood information with PointNet, PointNet++ [8] applied PointNet to individual patches of the local neighbourhood, and then stacked them together. PointCNN [17] further refined the PointNet framework with hierarchical \mathcal{X} -Conv which calculates inner products of \mathcal{X} -transformation and convolution filters of point clouds. Dynamic graph CNN (DGCNN) [6] adopted the graph neural network framework to incorporate local neighbourhood information by applying convolutions over the graph edges and dynamically updating graph for each layer. Furthermore, the tangent convolution architecture [18] incorporated 3D surface geometry by projecting point clouds on local tangent plane, and then applying convolution filters.

Varifolds. Geometric measure theory provides various tools for understanding, characterising and analysing surface geometry in various contexts, e.g., currents [12], varifolds [13, 15, 16] or normal cycles [19]. Despite their potential use for many applications, few studies have explored real-world applications of varifolds in the context of non-rigid surface registration [13].

3 Varifold representations for point clouds

The notion of varifold arises in geometric measure theory in the context of finding a minimal surface spanning a given closed curve in \mathbb{R}^3 , which is known as Plateau’s problem [20]. Intuitively, the concept of a varifold extends the idea of a differentiable manifold by replacing the requirement for differentiability with the condition of rectifiability [21]. This modification enables the representation of more complex surfaces, including those with singularities. For instance, Figure 1 in [21] presents straightforward examples of varifolds. Let $\Omega \subset \mathbb{R}^n$ be an open set. A general oriented d -varifold V

on Ω is a non-negative Radon measure on the product space of Ω with the oriented Grassmannian $\tilde{G}(d, n)$. In this study, we focus on a specific class of varifolds, the rectifiable varifolds, which are concentrated on d -rectifiable sets and can represent non-smooth surfaces such as 3D cubes.

Definition 3.1 (Rectifiable oriented d -varifolds). Let $\Omega \subset \mathbb{R}^n$ be an open set, X be an oriented d -rectifiable set, and θ be a non-negative measurable function with $\theta > 0$ \mathcal{H}^d -almost everywhere in X . The rectifiable oriented d -varifold $V = v(\theta, X)$ in Ω is the Radon measure on $\Omega \times \tilde{G}(d, n)$ defined by $V = \theta \mathcal{H}_{X \cap \Omega}^d \otimes \delta_{T_x X}$, i.e.,

$$\int_{\Omega \times \tilde{G}(d, n)} \phi(x, T) d\mu(x, T) = \int_X \phi(x, T_x X) \theta(x) d\mathcal{H}^d(x), \quad \forall \phi \in C_0(\Omega \times \tilde{G}(d, n)),$$

where C_0 denotes the class of continuous functions vanishing at infinity.

The mass of a d -rectifiable varifold $V = v(\theta, X)$ is the measure $\|V\| = \theta \mathcal{H}_X^d$. The non-negative function θ is usually called multiplicity. We assume in the rest of the paper that $\theta = 1$ for simplicity.

Various metrics and topologies can be defined on the space of varifolds. The mass distance defined as follows is a possible choice for a metric:

$$d_{\text{mass}}(\mu, \nu) = \sup \left\{ \left| \int_{\Omega \times \tilde{G}(d, n)} \phi d\mu - \int_{\Omega \times \tilde{G}(d, n)} \phi d\nu \right|, \phi \in C_0(\Omega \times \tilde{G}(d, n)), \|\phi\|_\infty \leq 1 \right\}. \quad (1)$$

However, the mass distance is not well suited for point clouds. For example, given two varifolds associated with Dirac masses δ_ε and δ_0 , their distance remains bounded away from 0 as it is always possible to find a test function ϕ such that $|\phi(0) - \phi(\varepsilon)| = 2$, regardless of how close the two points are. The 1-Wasserstein distance is not a more suitable choice in our context since it cannot compare two varifold measures with different mass. For example, given two Dirac masses $(1 + \varepsilon)\delta_0$ and δ_0 , the 1-Wasserstein distance between them goes to infinity as $\varepsilon |\phi(0)| \rightarrow \infty$.

Definition 3.2 (Bounded Lipschitz distance). Being μ and ν two varifolds on a locally compact metric space (X, d) , we define

$$d_{\text{BL}}(\mu, \nu) = \sup \left\{ \left| \int_{\Omega \times \tilde{G}(d, n)} \phi d\mu - \int_{\Omega \times \tilde{G}(d, n)} \phi d\nu \right|, \phi \in C_0^1(\Omega \times \tilde{G}(d, n)), \|\phi\|_{\text{Lip}} \leq 1, \|\phi\|_\infty \leq 1 \right\}. \quad (2)$$

The bounded Lipschitz distance (flat distance) can handle both problems, we refer for more details to [22] and the references therein. Although the bounded Lipschitz distance d_{BL} can provide theoretical properties for comparing varifolds, in practice, there is no straightforward way to numerically evaluate it. Instead, the kernel approach has been used to evaluate and compare varifolds numerically [13, 14].

Proposition 3.3. [14]. Let k_{pos} and k_G be continuous positive definite kernels on \mathbb{R}^n and $\tilde{G}(d, n)$, respectively. Assume in addition that for any $x \in \mathbb{R}^n$, $k_{\text{pos}}(x, \cdot) \in C_0(\mathbb{R}^n)$. Then $k_{\text{pos}} \otimes k_G$ is a positive definite kernel on $\mathbb{R}^n \times \tilde{G}(d, n)$, and the reproducing kernel Hilbert space (RKHS) W associated with $k_{\text{pos}} \otimes k_G$ is continuously embedded in $C_0(\mathbb{R}^n \times \tilde{G}(d, n))$, i.e., there exists $c_W > 0$ such that for any $\phi \in W$, we have $\|\phi\|_\infty < c_W \|\phi\|_W$.

Let $\tau_W : W \mapsto C_0(\mathbb{R}^n \times \tilde{G}(d, n))$ be the continuous embedding given by Proposition 3.3 and τ_{W^*} be its adjoint. Then varifolds can be viewed as elements of the dual RKHS W^* . Let μ and ν be two varifolds. By the Hilbert norm of W^* , the pseudo-metric can be induced as follows

$$\begin{aligned} d_{W^*}(\mu, \nu)^2 &= \|\mu - \nu\|_{W^*}^2 \\ &= \|\mu\|_{W^*}^2 - 2\langle \mu, \nu \rangle_{W^*} + \|\nu\|_{W^*}^2. \end{aligned} \quad (3)$$

The above pseudo-metric (since τ_{W^*} is not injective in general) is associated with the RKHS W , and it provides an efficient way to compute varifold by separating the positional and Grassmannian components. Indeed, one can derive a bound with respect to d_{BL} if we further assume that RKHS W is continuously embedded into $C_0^1(\mathbb{R}^n \times \tilde{G}(d, n))$ [13], i.e.,

$$\|\mu - \nu\|_{W^*} = \sup_{\phi \in W, \|\phi\|_W \leq 1} \int_{\mathbb{R}^n \times \tilde{G}(d, n)} \phi d(\mu - \nu) \leq c_W d_{\text{BL}}(\mu, \nu).$$

Neural tangent kernel. The recent advances of neural network theory finds a link between kernel theory and over-parameterised neural networks [23, 24]. If a neural network has a large but finite width, the weights at each layer remain close to its initialisation. Given training data pairs $\{\mathbf{x}_i, y_i\}_{i=1}^M$, where $\mathbf{x}_i \in \mathbb{R}^{d_0}$ and $y_i \in \mathbb{R}$, let $f(\boldsymbol{\theta}; \mathbf{x}_i)$ be a fully connected neural network with L -hidden layers with inputs \mathbf{x}_i and parameters $\boldsymbol{\theta} = \{\mathbf{W}^{(0)}, \mathbf{b}^{(0)}, \dots, \mathbf{W}^{(L)}, \mathbf{b}^{(L)}\}$. Let d_h be the width of the neural network for each layer h . The neural network function f can be written recursively as

$$f^{(h)}(\mathbf{x}) = \mathbf{W}^{(h)} g^{(h)}(\mathbf{x}) + \mathbf{b}^{(h)}, \quad g^{(h+1)}(\mathbf{x}) = \varphi(f^{(h)}(\mathbf{x})), \quad h = 0, \dots, L, \quad (4)$$

where $g^{(0)}(\mathbf{x}) = \mathbf{x}$ and φ is a non-linear activation function.

Assume the weights $\mathbf{W}^{(h)} \in \mathbb{R}^{d_{h+1} \times d_h}$ and bias $\mathbf{b}^{(h)} \in \mathbb{R}^{d_h}$ at each layer h are initialised with Gaussian distribution $\mathbf{W}^{(h)} \sim \mathcal{N}(0, \sigma_\omega^2 / d_h)$ and $\mathbf{b}^{(h)} \sim \mathcal{N}(0, \sigma_b^2)$, respectively. Consider training a neural network by minimising the least square loss function

$$l(\boldsymbol{\theta}) = \frac{1}{2} \sum_{i=1}^M (f(\boldsymbol{\theta}; \mathbf{x}_i) - y_i)^2. \quad (5)$$

Suppose the least square loss $l(\boldsymbol{\theta})$ is minimised with an infinitesimally small learning rate, i.e., $\frac{d\boldsymbol{\theta}}{dt} = -\nabla l(\boldsymbol{\theta}(t))$. Let $\mathbf{u}(t) = (f(\boldsymbol{\theta}(t); \mathbf{x}_i))_{i \in [M]} \in \mathbb{R}^M$ be the neural network outputs on all \mathbf{x}_i at time t , and $\mathbf{y} = (y_i)_{i \in [M]}$ be the desired output. Then $\mathbf{u}(t)$ follows the evolution

$$\frac{d\mathbf{u}}{dt} = -\mathbf{H}(t)(\mathbf{u}(t) - \mathbf{y}), \quad (6)$$

where

$$\mathbf{H}(t)_{ij} = \left\langle \frac{\partial f(\boldsymbol{\theta}(t); \mathbf{x}_i)}{\partial \boldsymbol{\theta}}, \frac{\partial f(\boldsymbol{\theta}(t); \mathbf{x}_j)}{\partial \boldsymbol{\theta}} \right\rangle. \quad (7)$$

If the width of the neural network at each layer goes to infinity, i.e., $d_h \rightarrow \infty$, with a fixed training set, then $\mathbf{H}(t)$ remains unchanged. Under random initialisation of the parameters $\boldsymbol{\theta}$, $\mathbf{H}(0)$ converges in probability to a deterministic kernel \mathbf{H}^* – the “neural tangent kernel” (i.e., NTK) [23]. Indeed, with few known activation functions φ (e.g., ReLU), the neural tangent kernel \mathbf{H}^* can be computed by a closed-form solution recursively using Gaussian process [25, 24]. For each layer h , the corresponding covariance function is defined as

$$\Sigma^{(0)}(\mathbf{x}_i, \mathbf{x}_j) = \sigma_b^2 + \frac{\sigma_\omega^2}{d_0} \mathbf{x}_i \mathbf{x}_j^\top, \quad (8)$$

$$\Lambda^{(h)}(\mathbf{x}_i, \mathbf{x}_j) = \begin{bmatrix} \Sigma^{(h-1)}(\mathbf{x}_i, \mathbf{x}_i) & \Sigma^{(h-1)}(\mathbf{x}_i, \mathbf{x}_j) \\ \Sigma^{(h-1)}(\mathbf{x}_j, \mathbf{x}_i) & \Sigma^{(h-1)}(\mathbf{x}_j, \mathbf{x}_j) \end{bmatrix} \in \mathbb{R}^{2 \times 2}, \quad (9)$$

$$\Sigma^{(h)}(\mathbf{x}_i, \mathbf{x}_j) = \sigma_b^2 + \sigma_\omega^2 \mathbb{E}_{(u, v) \sim \mathcal{N}(0, \Lambda^{(h)})} [\varphi(u) \varphi(v)]. \quad (10)$$

In order to compute the neural tangent kernel, derivative covariance is defined as

$$\dot{\Sigma}^{(h)}(\mathbf{x}_i, \mathbf{x}_j) = \sigma_\omega^2 \mathbb{E}_{(u, v) \sim \mathcal{N}(0, \Lambda^{(h)})} [\dot{\varphi}(u) \dot{\varphi}(v)]. \quad (11)$$

Then, with $\Theta^{(0)}(\mathbf{x}_i, \mathbf{x}_j) = \Sigma^{(0)}(\mathbf{x}_i, \mathbf{x}_j)$, the neural tangent kernel at each layer $\Theta^{(h)}$ can be computed as follows

$$\Theta^{(h)}(\mathbf{x}_i, \mathbf{x}_j) = \Sigma^{(h)}(\mathbf{x}_i, \mathbf{x}_j) + \Theta^{(h-1)} \dot{\Sigma}^{(h-1)}(\mathbf{x}_i, \mathbf{x}_j). \quad (12)$$

The convergence of $\Theta^{(L)}(\mathbf{x}_i, \mathbf{x}_j)$ to \mathbf{H}_{ij}^* is proven in Theorem 3.1 in [24].

3.1 Neural varifold computation

In this section, we present the kernel representation of varifold on point clouds via neural tangent kernel. We first introduce the neural tangent kernel representation of popular neural networks on point clouds [7, 24] by computing the neural tangent kernel for position and Grassmannian components, individually.

Given the set of \hat{n} point clouds $\mathcal{S} = \{s_1, s_2, \dots, s_{\hat{n}}\}$, where each point cloud $s_i = \{p_1, p_2, \dots, p_{\hat{m}}\}$ is a set of points, and \hat{n}, \hat{m} are respectively the number of point clouds and the number of points in each point cloud. Note that the number of points in each point cloud needs not be the same (e.g., $|s_1| \neq |s_2|$). For simplicity, we below assume different point clouds have the same number of points. Consider PointNet-like architecture that consists of L -hidden layers fully connected neural network shared by all points. For $(\hat{i}, \hat{j}) \in [\hat{m}] \times [\hat{m}]$, the covariance matrix $\Sigma^{(h)}(p_{\hat{i}}, p_{\hat{j}})$ and neural tangent kernel $\Theta^{(h)}(p_{\hat{i}}, p_{\hat{j}})$ at layer h are defined and computed in the same way of Equations (10) and (12). Assuming each point $p_{\hat{i}}$ consists of positional information and surface normal direction such that $p_{\hat{i}} \in \mathbb{R}^3 \times \mathbb{S}^2$, the varifold representation can be defined with neural tangent kernel theory in two different ways. One way is to follow the Charon-Trouvé approach [13] by computing the position and Grassmannian kernels separately. While the original Charon-Trouvé approach uses the radial basis kernel for the positional elements and a Cauchy-Binet kernel for the Grassmannian parts, in our cases, we use the neural tangent kernel representation for both the positional and Grassmannian parts. Let $p_{\hat{i}} = \{x_{\hat{i}}, z_{\hat{i}}\} \in \mathbb{R}^3 \times \mathbb{S}^2$ be a pair of position $x_{\hat{i}} \in \mathbb{R}^3$ and its surface normal $z_{\hat{i}} \in \mathbb{S}^2$, $\hat{i} = 1, \dots, \hat{m}$. The neural varifold representation is defined as

$$\Theta^{\text{varifold}}(p_{\hat{i}}, p_{\hat{j}}) = \Theta^{\text{pos}}(x_{\hat{i}}, x_{\hat{j}}) \cdot \Theta^G(z_{\hat{i}}, z_{\hat{j}}). \quad (13)$$

We refer the above representation as PointNet-NTK1. As shown in Corollary 3.4 below, PointNet-NTK1 is a valid Charon-Trouvé type kernel. From the neural tangent theory of view, PointNet-NTK1 in Equation (13) has two infinite-width neural networks on positional and Grassmannian components separately, and then aggregates information from the neural networks by element-wise product of the two neural tangent kernels.

Corollary 3.4. *In the limit of resolution going to infinity, neural tangent kernels Θ^{pos} and Θ^G are continuous positive definite kernels on positions and tangent planes, respectively. The varifold kernel $\Theta^{\text{varifold}} = \Theta^{\text{pos}} \odot \Theta^G$ is a positive definite kernel on $\mathbb{R}^n \times \tilde{G}(d, n)$ and the associated RKHS W is continuously embedded into $C_0(\mathbb{R}^n \times \tilde{G}(d, n))$.*

The other way to define a varifold representation is by treating each point as a 6-dimensional feature $p_{\hat{i}} = \{x_{\hat{i}}, z_{\hat{i}}\} \in \mathbb{R}^6$. In this case, a single neural tangent kernel corresponding to an infinite-width neural network can be used, i.e.,

$$\Theta^{\text{varifold}}(p_{\hat{i}}, p_{\hat{j}}) = \Theta(\{x_{\hat{i}}, z_{\hat{i}}\}, \{x_{\hat{j}}, z_{\hat{j}}\}). \quad (14)$$

We refer it as PointNet-NTK2. Since PointNet-NTK2 does not compute the positional and Grassmannian kernels separately, it is computationally cheaper than PointNet-NTK1. It cannot be associated in the limit with a Charon-Trouvé type kernel, in contrast with PointNet-NTK1, but it remains theoretically well grounded because the explicit coupling of positions and normals is a key aspect of the theory of varifolds that provides strong theoretical guarantees (e.g., convergence, compactness, weak regularity, second-order information, etc.). Furthermore, PointNet-NTK2 falls into the category of neural networks proposed for point clouds [7, 8] that treat point positions and surface normals as 6-feature vectors, and thus PointNet-NTK2 is a natural extension of current neural networks practices for point clouds.

PointNet-NTK1 and PointNet-NTK2 in Equations (13) and (14) are computing NTK values between two points $p_{\hat{i}}$ and $p_{\hat{j}}$. The above forms can compute only pointwise-relationship in a single point cloud. However, in many point cloud applications, two or more point clouds need to be evaluated. Given the set of point clouds \mathcal{S} , one needs to compute a Gram matrix of size $\hat{n} \times \hat{n} \times \hat{m} \times \hat{m}$, which is computationally prohibitive in general. In order to reduce the size of the Gram matrix, we aggregate information by summation/average in all elements of Θ^{varifold} , thus forming an $\hat{n} \times \hat{n}$ matrix, i.e.,

$$\Theta^{\text{varifold}}(s_i, s_j) = \sum_{\hat{i} \leq \hat{m}} \sum_{\hat{j} \leq \hat{m}} \Theta^{\text{varifold}}(p_{\hat{i}} \in s_i, p_{\hat{j}} \in s_j). \quad (15)$$

Analogous to Equation (3), the varifold representation Θ^{varifold} can be used as a shape similarity metric between two sets of point clouds s_i and s_j . The varifold metric can be computed as follows

$$\|s_i - s_j\|_{\text{varifold}}^2 = \Theta^{\text{varifold}}(s_i, s_j) - 2\Theta^{\text{varifold}}(s_i, s_j) + \Theta^{\text{varifold}}(s_i, s_j). \quad (16)$$

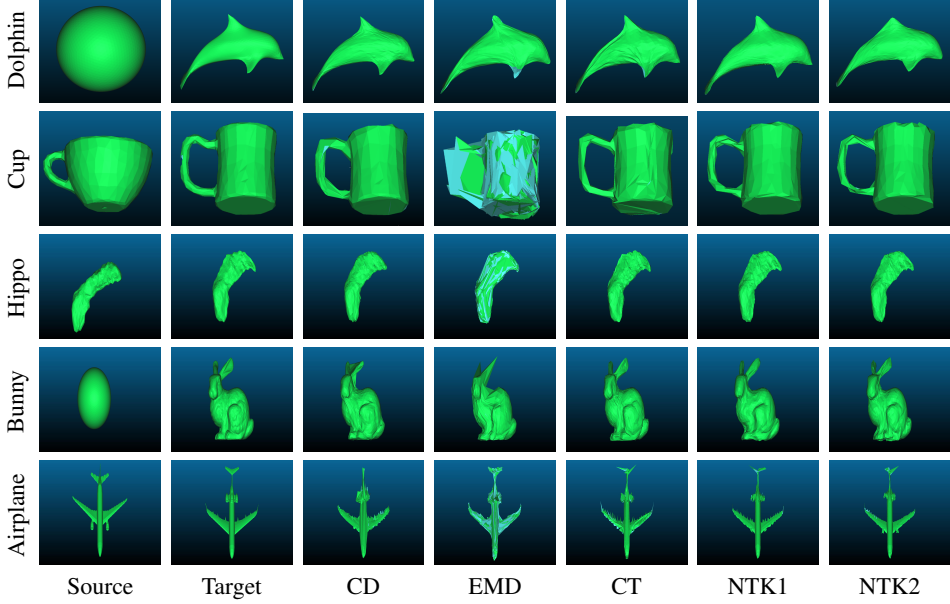


Figure 1: Shape matching examples with different shape similarity metrics, i.e., CD, EMD, CT, NTK1 and NTK2. Hippo is a shortened term referring to the hippocampus.

Furthermore, the varifold representation can be used for shape classification or any regression with the labels on point clouds data. Given training and test point cloud sets and their label pairs $(\chi_{\text{train}}, \mathcal{Y}_{\text{train}}) = \{(s_1, y_1), \dots, (s_l, y_l)\}$ and $(\chi_{\text{test}}, \mathcal{Y}_{\text{test}}) = \{(s_{l+1}, y_{l+1}), \dots, (s_{\hat{n}}, y_{\hat{n}})\}$, then neural varifold and its norm can be reformulated to predict labels using kernel ridge regression, i.e.,

$$\mathcal{Y}_{\text{test}} = \Theta_{\text{test}}^{\text{varifold}}(\chi_{\text{test}}, \chi_{\text{train}})(\Theta_{\text{train}}^{\text{varifold}}(\chi_{\text{train}}, \chi_{\text{train}}) + \lambda \mathbf{I})^{-1} \mathcal{Y}_{\text{train}}, \quad (17)$$

where λ is the regularisation parameter.

4 Experiments

Dataset and experimental setting. We evaluate the varifold kernel representations and conduct comparisons on three different sought-after tasks: point cloud based shape matching between two different 3D meshes, point cloud based few-shot shape classification, and point cloud based 3D shape reconstruction. The details of each experiment setup are available at Appendix A.1, and the high-level pseudo-codes for each task are available at Appendix A.4. For ease of reference, we below shorten PointNet-NTK1, PointNet-NTK2, Chamfer distance, Charon-Trouvé varifold norm and Earth Mover’s distance as NTK1, NTK2, CD, CT and EMD, respectively.

4.1 Shape matching

To evaluate the surface representation using neural varifolds and make comparison with existing shape similarity metrics, synthetic shape matching experiments are conducted. We train MLP networks with 2 hidden layers with width of 64 and 128 units respectively. These networks use various shape similarity metrics as loss functions to deform the given source shape into the target shape (more details are available at Appendix A.1.1).

Figure 1 shows five examples of shape matching based on various shape similarity metric losses. The neural network trained with CD captures geometric details well, except for the airplane. For hippocampi, CD over smoothes sharp edges; and for the bunny, it over smoothes the ears. While CD matches airplane wing shapes, it is noisier than CT, NTK1, and NTK2 methods. The EMD-trained network performs well on the dolphin shape but struggles with geometric details and surface consistency for other shapes, likely due to insufficient parameters for the transportation plan. More iterations and a lower convergence threshold make training inefficient. Networks trained with NTK1 and NTK2 metrics penalise broken meshes and surface noise, resulting in better mesh quality. NTK2

over smooths high-frequency features on the dolphin, while NTK1 achieves good results. NTK1 and NTK2 show superior shape matching for airplane fuselage and wings. The network trained with CT gives acceptable results except for the airplane; however, one main disadvantage is that CT’s radial basis kernel is sensitive to point cloud density, requiring hyperparameter σ adjustments for each pair of point clouds to avoid poor results.

Table 1 presents the quantitative evaluation of the shape matching task. Each column indicates that the shape matching neural network is trained with a specific shape similarity metric as the loss function. In the case of dolphin, when the evaluation metric is the same as the loss function used to train the network, the network trained with the same evaluation metric achieves the best results. This is natural as the neural network is trained to minimise the loss function. It is worth highlighting that the shape matching network trained with the NTK1 loss achieves the second best score for all evaluation metrics except for itself. In other words, NTK1 can capture common characteristics of all shape similarity metrics used to train the network. Furthermore, in the case of shape matching between two different cups, our neural varifold metrics (NTK1 and NTK2) achieve either the best or second best results regardless which shape evaluation metric is used. This indicates that the neural varifold metrics can capture better geometric details as well as surface smoothness for the cup shape than other metrics. In the case of shape matching between the source hippocampus and the target hippocampus, the network trained with CT excels in the CD metric, while the network trained with NTK1 achieves superior results with respect to NTK1 and NTK2 metrics. The shape matching network trained with NTK2 outperforms in the EMD, CT and NTK2 metrics. In the case of the bunny, CT shows the best results with respect to CD and CT, while NTK1 shows the best matching results with respect to EMD and NTK1. NTK2, on the other hand, shows the second best results with respect to all metrics except for itself. In the case of airplane, CT shows the best matching results with respect to CD, EMD and CT. However, the CT metric itself shows the negative value, i.e. unstable. This is mainly because the RBF kernel used in CT is badly scaled. NTK1 shows the second best shape matching results with respect to all metrics except for itself. The detailed analysis for the role of the NTK layers on shape matching is available at Appendix A.5.2.

4.2 Few-shot shape classification

In this section, the proposed NTKs are firstly compared with the current state-of-the-art few-shot classification methods on the ModelNet40-FS benchmark [26]. ModelNet40-FS benchmark [26] divided different shape categories in ModelNet40 datasets for pre-training the network with 30 classes and then evaluated few-shot shape classification on 10 classes. The experiment was conducted in the standard few-shot learning setup, i.e. N-way K-shot Q-query. The definition of N-way K-shot Q-query is available at Appendix A.1. Table 2 shows the shape classification results on two different few-shot classification setups, i.e., 5way-1shot-15query and 5way-5shot-15query. In the case of the 5way-1shot classification, the current state-of-the-art method PCIA achieves the best results by

Table 1: Results of shape matching deforming the given source shapes into the target shapes using a neural network trained with various shape similarity metrics. Metrics used in columns and rows are to train the neural network and for quantitative evaluation, respectively. Every value indicates the shape matching distance. In particular, the lowest and second lowest values (i.e., the best and the second best) in each row are highlighted in bold and underscored, respectively.

	Metric	CD	EMD	CT	NTK1	NTK2
Dolphin	CD	2.49E-4	3.39E-4	2.90E-4	2.84E-4	3.04E-4
	EMD	7.56E0	3.87E0	4.15E0	4.13E0	4.27E0
	CT	3.76E-2	2.94E-2	1.22E-2	<u>1.63E-2</u>	1.95E-2
	NTK1	6.56E-3	1.89E-3	2.93E-3	4.82E-4	6.34E-4
	NTK2	1.72E-2	4.33E-3	9.99E-3	<u>1.34E-3</u>	1.25E-3
Cup	CD	4.55E-3	9.74E-3	4.13E-3	3.26E-3	3.36E-3
	EMD	2.03E1	3.53E1	2.06E1	1.85E1	1.79E1
	CT	6.90E-1	2.85E0	4.07E-1	<u>3.29E-1</u>	3.20E-1
	NTK1	1.72E-2	7.27E-1	1.97E-2	6.07E-3	6.50E-3
	NTK2	3.14E-2	3.29E0	4.53E-2	<u>1.34E-2</u>	1.21E-2
Hippocampus	CD	3.49E-1	3.2E-1	2.43E-1	2.67E-1	2.65E-1
	EMD	2.80E5	2.10E5	2.25E5	<u>2.09E5</u>	1.96E5
	CT	2.27E3	2.92E5	2.32E3	2.19E3	2.15E3
	NTK1	1.84E5	1.01E9	59.7E5	4.93E3	9.98E3
	NTK2	6.37E4	3.09E9	1.56E6	1.54E3	1.54E3
Bunny	CD	9.32E-3	5.12E-3	3.60E-3	4.40E-3	4.32E-3
	EMD	2.31E4	4.74E3	3.72E3	3.13E3	<u>3.52E3</u>
	CT	2.40E-1	1.25E0	7.51E-2	1.28E-1	1.23E-1
	NTK1	2.57E-2	1.32E-2	1.83E-3	2.22E-4	2.94E-4
	NTK2	3.85E-2	2.68E-2	3.33E-3	8.85E-4	6.43E-4
Airplane	CD	1.36E-3	4.07E-4	3.72E-3	<u>3.81E-3</u>	5.90E-3
	EMD	1.16E4	4.12E2	3.38E2	<u>3.43E2</u>	7.50E2
	CT	8.71E-2	3.62E0	-3.58E-4	1.67E-3	3.68E-3
	NTK1	2.27E-3	1.80E-1	0.41E-6	0.31E-6	0.72E-6
	NTK2	6.14E-2	5.13E0	8.69E-6	3.17E-6	2.42E-6

around 7% margin in comparison to the second best method NTK2 (pre-trained). In the case of the 5way-5shot classification, NTK2 outperforms PCIA by around 0.8% margin. Note that PCIA requires to train backbone networks with PCIA modules and needs to fix the size of query. NTKs, on the other hand, can directly use the extracted backbone network features without further training the few-shot layer weights and do meta-learning in any arbitrary N-way K-shot Q-query settings. If NTKs are used without pre-trained backbone features, i.e., directly using positional and normal coordinates, then the results are subpar in comparison to other meta-learning approaches. This is understandable as few-shot architectures built on top of the backbone features, while NTKs without a pre-trained model, can only access the raw features, and thus cannot take advantages of the powerful feature learning capability of the neural networks. Interestingly, NTK1 outperforms NTK2 without pre-trained features, while NTK2 (DGCNN) outperforms NTK1 (DGCNN). This is because we use the pre-trained DGCNN on point clouds with spatial coordinates (x,y,z) as a backbone network for extracting both positional and normal features. Relatively low performance on NTK1 (DGCNN) is mainly because there is no appropriate architecture treating position and normal features separately.

Small-data tasks are common when data is limited. In the shape classification experiment, we restrict data availability and assume no pre-trained models, requiring training with 1, 5, 10, or 50 samples. Table 3 shows ModelNet classification accuracy with limited samples. Kernel-based approaches excel in small-data tasks. In particular, with only one sample, kernel methods outperform finite-width neural networks like PointNet and DGCNN on both ModelNet10 and ModelNet40, with NTK2 and NTK1 achieving the best results, respectively. Interestingly, the CT kernel performs as well as NTK1 and NTK2 on ModelNet10 but drops significantly on ModelNet40. Similar results occur with five samples: NTK1 and NTK2 achieve 81.3% and 81.7% on ModelNet10, while CT, PointNet, and DGCNN lag by 3.1%, 5.1%, and 5.9%, respectively. On ModelNet40, NTK1 outperforms all other methods more significantly than on ModelNet10. As the number of training samples increases, finite-width neural networks significantly improve their performance on both ModelNet10 and ModelNet40. With ten samples, NTK1 and NTK2 achieve around 86.1% accuracy, outperforming other methods on ModelNet10 by 2–3%, although DGCNN surpasses NTK and PointNet on ModelNet40. With 50 samples, PointNet and DGCNN outperform NTK approaches by about 1% on ModelNet10 and 3–5% on ModelNet40. NTK1 and NTK2 show similar performance on ModelNet10 (with 0.3% difference), while NTK1 slightly outperforms NTK2 on ModelNet40 by 0.6–1.6%. Notably, NTK1 and NTK2 consistently outperform the CT varifold kernel.

Kernel-based learning is known for its quadratic computational complexity. However, NTK1 and NTK2 are computationally competitive in both few-shot learning and limited data scenarios. For instance, training NTK1 and NTK2 on ModelNet10 with 5 samples takes 47 and 18 seconds, respectively, compared to 254 and 502 seconds for training PointNet and DGCNN for 250 epochs on a single 3090 GPU. The shape classification performance on the full ModelNet data is available at App-

Table 2: Few-shot shape classification comparison on the ModelNet40-FS classification benchmark in terms of two setups, i.e., 5way-1shot and 5way-5shot. Every value indicates the mean shape classification accuracy with 95% confidence interval. NTK1 (DGCNN) and NTK2 (DGCNN) imply that, instead of point clouds positions and their normals, point-wise features from the pre-trained DGCNN are used for our NTK1 and NTK2.

Methods	ModelNet40-FS	
	5way-1shot	5way-5shot
Prototypical Net	69.96 ± 0.67	85.51 ± 0.52
Relation Net	68.57 ± 0.73	82.01 ± 0.53
PointBERT	69.41 ± 3.16	86.83 ± 2.03
PCIA *	82.21 ± 0.76	89.42 ± 0.53
NTK1	64.94 ± 0.84	83.42 ± 0.59
NTK2	62.67 ± 0.81	81.53 ± 0.59
NTK1 (DGCNN)	69.30 ± 0.76	86.75 ± 0.51
NTK2 (DGCNN)	75.23 ± 0.71	90.20 ± 0.49

* Point cloud inputs are positions and unit normal vectors, i.e., 6-feature vectors. Note that the original paper’s reported accuracy for 5way-1shot and 5way-5shot is 81.19% and 89.30%, respectively.

Table 3: ModelNet classification with limited training samples selected randomly. Every value indicates the average classification accuracy with standard deviation from 20 times iterations.

Methods	1-sample	5-sample	10-sample	50-sample
	ModelNet10			
PointNet	38.84 ± 6.41	76.57 ± 2.28	84.14 ± 1.43	91.42 ± 0.89
DGCNN	33.56 ± 4.60	75.81 ± 2.40	83.90 ± 1.70	91.54 ± 0.68
CT	59.06 ± 4.76	78.64 ± 2.90	83.35 ± 1.57	87.98 ± 0.79
NTK1	59.49 ± 4.80	81.34 ± 2.78	86.07 ± 1.62	90.18 ± 0.93
NTK2	59.64 ± 5.50	81.74 ± 3.15	86.12 ± 1.56	90.10 ± 0.73
	ModelNet40			
	PointNet	33.11 ± 3.28	63.30 ± 2.12	73.63 ± 1.06
DGCNN		36.04 ± 3.22	67.49 ± 1.80	77.04 ± 0.81
CT		37.71 ± 3.42	60.43 ± 1.51	67.13 ± 1.11
NTK1		44.03 ± 3.51	69.30 ± 1.48	75.81 ± 1.23
NTK2		42.85 ± 3.51	67.81 ± 1.47	74.62 ± 1.00

pendix A.3. Ablation study regarding the criteria used to choose the number of layers and different layer width for NTKs is available at Appendix A.5.

4.3 Shape reconstruction

Shape reconstruction from point clouds is tested for NTK1, SIREN, neural splines, and NKS. NTK2 is excluded as it is unsuitable for this task. Implementation details are in Appendix A.2. Reconstruction quality is evaluated with CD and EMD metrics. Figure 2 shows examples (e.g., airplane and cabinet) with 2048 points. NTK1 performs better in surface completion and smoothness. Additional visualizations are in Appendix A.6.

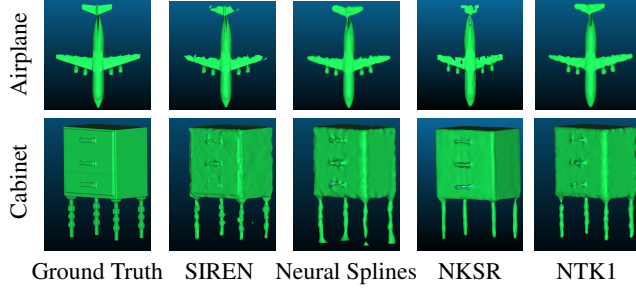


Figure 2: Examples of the shape reconstruction comparison.

the best reconstruction results for the rest 6 categories. NTK1 based reconstruction achieves the lowest mean EMD for vessel and cabinet, while neural splines and SIREN achieve the lowest mean EMD for 7 and 5 categories, respectively. NKS does not achieve the lowest mean CD and EMD for all the categories. In addition, the shape reconstruction results with different number of points (i.e., 512 and 1024) are available at Appendix A.5.4.

SIREN shows the lowest distance for both CD and EMD followed by NTK1. Surprisingly, the neural splines method underperforms in both the CD and EMD when we consider all the 13 categories. The performance of NTK1 on shape reconstruction is clearly comparable with these state-of-the-art methods. This might be counter-intuitive as it regularises the kernel with additional normal information, this is probably because there is no straightforward way to assign normals on the regular grid coordinates, where the signed distance values are estimated by the kernel regression.

Table 4: ShapeNet 3D mesh reconstruction with 2048 points (mean/median values $\times 1E3$). NS: Neural Splines.

Metric	Method	Airplane	Bench	Cabinet	Car	Chair	Display	Lamp	Speaker	Rifle	Sofa	Table	Phone	Vessel
CD (mean)	SIREN	1.501	1.624	2.430	2.725	1.556	2.193	1.392	7.906	1.212	1.734	1.856	1.478	2.557
	NS	4.145	1.304	1.969	2.131	1.828	4.577	1.062	2.798	0.400	1.650	1.576	10.058	2.210
	NKS	1.141	2.000	2.423	2.198	2.520	17.720	5.477	3.622	0.414	1.848	2.493	1.547	1.093
	NTK1	0.644	1.314	1.991	2.107	1.734	4.666	1.134	2.806	0.425	1.654	1.586	10.397	1.079
CD (median)	SIREN	0.733	1.384	2.153	2.134	1.230	1.469	0.661	3.304	0.581	1.706	1.670	1.424	1.112
	NS	0.947	1.289	1.799	1.640	1.160	1.413	0.479	2.749	0.347	1.586	1.372	1.600	0.788
	NKS	1.205	1.426	1.797	1.830	1.236	1.565	1.579	2.945	0.326	1.638	1.637	1.305	0.894
	NTK1	0.621	1.259	1.828	1.836	1.237	1.499	0.566	2.794	0.352	1.578	1.350	1.558	0.797
EMD (mean)	SIREN	2.990	3.763	4.983	5.208	4.649	4.658	24.068	13.292	2.418	3.688	8.745	3.237	4.500
	NS	22.004	3.571	4.420	4.694	7.916	9.205	16.786	5.857	1.503	3.706	4.194	17.846	5.957
	NKS	7.153	8.456	8.018	8.190	16.824	31.182	21.182	9.984	2.329	5.871	13.658	4.152	4.581
	NTK1	3.120	4.153	4.420	4.767	7.350	9.653	23.381	6.236	1.592	3.888	5.259	24.101	3.534
EMD (median)	SIREN	2.690	2.938	4.520	3.803	4.411	3.314	2.279	6.240	1.605	3.653	3.782	3.060	2.576
	NS	6.873	3.068	4.154	3.999	4.740	4.053	3.802	5.123	1.216	3.543	3.695	3.838	2.210
	NKS	5.732	5.119	4.440	5.313	5.683	3.777	4.927	5.975	1.227	3.641	6.375	3.088	2.771
	NTK1	2.864	3.319	4.284	3.947	5.293	3.875	3.288	5.795	1.271	3.738	3.980	3.380	2.074

5 Limitations

While the proposed neural varifold has advantages over standard baselines, it has limitations. First, it is based on the simpler PointNet architecture. Future research should explore its performance with more advanced architectures like graph convolutions or voxelised point clouds. Second, the quadratic computational complexity of the kernel regime poses a challenge for large datasets. Kernel approximation methods, such as Nyström approximation, could reduce this complexity, and their performance compared to exact kernels should be evaluated.

Quantitatively, Table 4 shows the mean and median of using the CD and EMD for 20 shapes randomly selected from each of the 13 different shape categories in the ShapeNet dataset. For the CD, NTK1 shows the best average reconstruction results for the airplane, cabinet, car and vessel categories; SIREN shows the best reconstruction results for the chair, display and phone categories; and the neural splines method shows

References

- [1] J. Deng, S. Shi, P. Li, W. Zhou, Y. Zhang, and H. Li, “Voxel r-cnn: Towards high performance voxel-based 3d object detection,” in *Proceedings of the AAAI conference on artificial intelligence*, vol. 35, pp. 1201–1209, 2021.
- [2] S. Shi, C. Guo, L. Jiang, Z. Wang, J. Shi, X. Wang, and H. Li, “Pv-rcnn: Point-voxel feature set abstraction for 3d object detection,” in *Proceedings of the IEEE/CVF conference on computer vision and pattern recognition*, pp. 10529–10538, 2020.
- [3] C. Choy, J. Gwak, and S. Savarese, “4d spatio-temporal convnets: Minkowski convolutional neural networks,” in *Proceedings of the IEEE/CVF conference on computer vision and pattern recognition*, pp. 3075–3084, 2019.
- [4] J. Bruna, W. Zaremba, A. Szlam, and Y. Lecun, “Spectral networks and locally connected networks on graphs,” in *International Conference on Learning Representations (ICLR2014), CBLS, April 2014*, 2014.
- [5] M. M. Bronstein, J. Bruna, Y. LeCun, A. Szlam, and P. Vandergheynst, “Geometric deep learning: going beyond Euclidean data,” *IEEE Signal Processing Magazine*, vol. 34, no. 4, pp. 18–42, 2017.
- [6] Y. Wang, Y. Sun, Z. Liu, S. E. Sarma, M. M. Bronstein, and J. M. Solomon, “Dynamic graph cnn for learning on point clouds,” *ACM Transactions on Graphics (TOG)*, vol. 38, no. 5, pp. 1–12, 2019.
- [7] C. R. Qi, H. Su, K. Mo, and L. J. Guibas, “Pointnet: Deep learning on point sets for 3d classification and segmentation,” in *Proceedings of the IEEE Conference on Computer Vision and Pattern Recognition*, pp. 652–660, 2017.
- [8] C. R. Qi, L. Yi, H. Su, and L. J. Guibas, “Pointnet++: Deep hierarchical feature learning on point sets in a metric space,” in *Advances in neural information processing systems*, pp. 5099–5108, 2017.
- [9] H. Thomas, C. R. Qi, J.-E. Deschaud, B. Marcotegui, F. Goulette, and L. J. Guibas, “Kpconv: Flexible and deformable convolution for point clouds,” in *Proceedings of the IEEE/CVF international conference on computer vision*, pp. 6411–6420, 2019.
- [10] M. Defferrard, X. Bresson, and P. Vandergheynst, “Convolutional neural networks on graphs with fast localized spectral filtering,” in *Advances in neural information processing systems*, pp. 3844–3852, 2016.
- [11] F. Monti, D. Boscaini, J. Masci, E. Rodola, J. Svoboda, and M. M. Bronstein, “Geometric deep learning on graphs and manifolds using mixture model cnns,” in *Proceedings of the IEEE Conference on Computer Vision and Pattern Recognition*, pp. 5115–5124, 2017.
- [12] M. Vaillant and J. Glaunès, “Surface matching via currents,” in *Biennial International Conference on Information Processing in Medical Imaging*, pp. 381–392, Springer, 2005.
- [13] N. Charon and A. Trouvé, “The varifold representation of nonoriented shapes for diffeomorphic registration,” *SIAM Journal on Imaging Sciences*, vol. 6, no. 4, pp. 2547–2580, 2013.
- [14] H.-W. Hsieh and N. Charon, “Metrics, quantization and registration in varifold spaces,” *Found. Comput. Math.*, vol. 21, no. 5, pp. 1317–1361, 2021.
- [15] B. Buet, G. P. Leonardi, and S. Masnou, “A varifold approach to surface approximation,” *Archive for Rational Mechanics and Analysis*, vol. 226, no. 2, pp. 639–694, 2017.
- [16] B. Buet, G. P. Leonardi, and S. Masnou, “Weak and approximate curvatures of a measure: a varifold perspective,” *Nonlinear Analysis*, vol. 222: paper no 112983, 34, 2022.
- [17] Y. Li, R. Bu, M. Sun, W. Wu, X. Di, and B. Chen, “Pointcnn: Convolution on x-transformed points,” in *Advances in neural information processing systems*, pp. 820–830, 2018.
- [18] M. Tatarchenko, J. Park, V. Koltun, and Q.-Y. Zhou, “Tangent convolutions for dense prediction in 3d,” in *Proceedings of the IEEE Conference on Computer Vision and Pattern Recognition*, pp. 3887–3896, 2018.
- [19] P. Roussillon and J. A. Glaunès, “Representation of surfaces with normal cycles and application to surface registration,” *Journal of Mathematical Imaging and Vision*, vol. 61, no. 8, pp. 1069–1095, 2019.

- [20] W. K. Allard, “On the first variation of a varifold: boundary behavior,” *Annals of Mathematics*, pp. 418–446, 1975.
- [21] B. Buet, “Varifolds and generalized curvature,” in *ESAIM: Proceedings*, vol. 42, pp. 1–9, EDP Sciences, 2013.
- [22] B. Piccoli and F. Rossi, “On properties of the generalized wasserstein distance,” *Archive for Rational Mechanics and Analysis*, vol. 222, no. 3, pp. 1339–1365, 2016.
- [23] A. Jacot, F. Gabriel, and C. Hongler, “Neural tangent kernel: Convergence and generalization in neural networks,” in *Advances in neural information processing systems*, pp. 8571–8580, 2018.
- [24] S. Arora, S. S. Du, W. Hu, Z. Li, R. R. Salakhutdinov, and R. Wang, “On exact computation with an infinitely wide neural net,” in *Advances in Neural Information Processing Systems*, pp. 8139–8148, 2019.
- [25] J. Lee, Y. Bahri, R. Novak, S. S. Schoenholz, J. Pennington, and J. Sohl-Dickstein, “Deep neural networks as Gaussian processes,” *arXiv preprint arXiv:1711.00165*, 2017.
- [26] C. Ye, H. Zhu, B. Zhang, and T. Chen, “A closer look at few-shot 3d point cloud classification,” *International Journal of Computer Vision*, pp. 772–795, 2023.
- [27] N. Ravi, J. Reizenstein, D. Novotny, T. Gordon, W.-Y. Lo, J. Johnson, and G. Gkioxari, “Accelerating 3d deep learning with PyTorch3D,” *arXiv:2007.08501*, 2020.
- [28] P. H. Martin Bauer, Nicolas Charon and H.-W. Hsieh, “A numerical framework for elastic surface matching, comparison, and interpolation,” 2020. Preprint available on ArXiv.
- [29] B. Charlier, J. Feydy, J. A. Glaunes, F.-D. Collin, and G. Durif, “Kernel operations on the gpu, with autodiff, without memory overflows,” *The Journal of Machine Learning Research*, vol. 22, no. 1, pp. 3457–3462, 2021.
- [30] J. Snell, K. Swersky, and R. Zemel, “Prototypical networks for few-shot learning,” *Advances in neural information processing systems*, vol. 30, 2017.
- [31] F. Sung, Y. Yang, L. Zhang, T. Xiang, P. H. Torr, and T. M. Hospedales, “Learning to compare: Relation network for few-shot learning,” in *Proceedings of the IEEE conference on computer vision and pattern recognition*, pp. 1199–1208, 2018.
- [32] X. Yu, L. Tang, Y. Rao, T. Huang, J. Zhou, and J. Lu, “Point-bert: Pre-training 3d point cloud transformers with masked point modeling,” in *Proceedings of the IEEE/CVF Conference on Computer Vision and Pattern Recognition*, pp. 19313–19322, 2022.
- [33] R. Novak, L. Xiao, J. Hron, J. Lee, A. A. Alemi, J. Sohl-Dickstein, and S. S. Schoenholz, “Neural tangents: Fast and easy infinite neural networks in Python,” in *International Conference on Learning Representations*, 2020.
- [34] Z. Wu, S. Song, A. Khosla, F. Yu, L. Zhang, X. Tang, and J. Xiao, “3d shapenets: A deep representation for volumetric shapes,” in *Proceedings of the IEEE conference on computer vision and pattern recognition*, pp. 1912–1920, 2015.
- [35] A. X. Chang, T. Funkhouser, L. Guibas, P. Hanrahan, Q. Huang, Z. Li, S. Savarese, M. Savva, S. Song, H. Su, et al., “Shapenet: An information-rich 3d model repository,” *arXiv preprint arXiv:1512.03012*, 2015.
- [36] F. Williams, M. Trager, J. Bruna, and D. Zorin, “Neural splines: Fitting 3d surfaces with infinitely-wide neural networks,” in *Proceedings of the IEEE/CVF Conference on Computer Vision and Pattern Recognition*, pp. 9949–9958, 2021.
- [37] V. Sitzmann, J. Martel, A. Bergman, D. Lindell, and G. Wetzstein, “Implicit neural representations with periodic activation functions,” *Advances in neural information processing systems*, vol. 33, pp. 7462–7473, 2020.
- [38] J. Huang, Z. Gojcic, M. Atzmon, O. Litany, S. Fidler, and F. Williams, “Neural kernel surface reconstruction,” in *Proceedings of the IEEE/CVF Conference on Computer Vision and Pattern Recognition*, pp. 4369–4379, 2023.
- [39] M. Liu, L. Sheng, S. Yang, J. Shao, and S.-M. Hu, “Morphing and sampling network for dense point cloud completion,” in *Proceedings of the AAAI conference on artificial intelligence*, vol. 34, pp. 11596–11603, 2020.

- [40] S. Cuomo, A. Galletti, G. Giunta, and A. Starace, “Surface reconstruction from scattered point via RBF interpolation on GPU,” in *2013 federated conference on computer science and information systems*, pp. 433–440, IEEE, 2013.
- [41] W. E. Lorensen and H. E. Cline, “Marching cubes: A high resolution 3d surface construction algorithm,” in *Seminal graphics: pioneering efforts that shaped the field*, pp. 347–353, 1998.
- [42] T. Lewiner, H. Lopes, A. W. Vieira, and G. Tavares, “Efficient implementation of marching cubes’ cases with topological guarantees,” *Journal of graphics tools*, vol. 8, no. 2, pp. 1–15, 2003.
- [43] J. Lee, S. Schoenholz, J. Pennington, B. Adlam, L. Xiao, R. Novak, and J. Sohl-Dickstein, “Finite versus infinite neural networks: an empirical study,” *Advances in Neural Information Processing Systems*, vol. 33, pp. 15156–15172, 2020.
- [44] Y. Cho and L. Saul, “Kernel methods for deep learning,” *Advances in neural information processing systems*, vol. 22, 2009.
- [45] J. Lee, L. Xiao, S. Schoenholz, Y. Bahri, R. Novak, J. Sohl-Dickstein, and J. Pennington, “Wide neural networks of any depth evolve as linear models under gradient descent,” *Advances in neural information processing systems*, vol. 32, 2019.
- [46] J. Hron, Y. Bahri, J. Sohl-Dickstein, and R. Novak, “Infinite attention: Nngp and ntk for deep attention networks,” in *International Conference on Machine Learning*, pp. 4376–4386, PMLR, 2020.
- [47] R. Novak, J. Sohl-Dickstein, and S. S. Schoenholz, “Fast finite width neural tangent kernel,” in *International Conference on Machine Learning*, pp. 17018–17044, PMLR, 2022.

A Appendix

A.1 Experimental setup

A.1.1 Shape matching

For point cloud based shape matching, MLP networks consisting of 2 hidden layers (with width size of 64 and 128, respectively) were trained for computing displacement between two shapes, such that one can deform the source shape to the target shape. The neural networks were trained with different shape similarity metric losses including neural varifold. Point clouds of the given shapes were extracted by collecting the centre of triangular meshes of the given shapes, and the corresponding normals were computed by cross product of two edges of the meshes. The first example is deforming the source unit sphere into the target dolphin shape; the second is matching two different cup designs; the third is matching between two hippocampi; the fourth is the shape matching bewteen sphere and Stanford bunny; and the fifth is the shape matching between two different designs of airplane. The data is acquired from the PyTorch3D, SRNFmatch and KeOps GitHub repositories [27, 28, 29]. This experiment evaluates how well the source shape can be deformed based on the chosen shape similarity measure as the loss function. A simple 3-layer MLP network was solely trained with a single shape similarity measure loss, with the learning rate fixed to 1E-3 and the Adam optimiser. The network was trained with popular shape similarity measures including the CD (Chamfer distance), EMD (Earth Mover’s distance), CT (Charon-Trouvé varifold norm), and the proposed neural varifold norms (NTK1 and NTK2). In the case of CD and EMD, we followed the same method used for shape reconstruction. For varifold metrics, we used Equation (16); note that it is a squared distance commonly used for optimisation. For the numerical evaluation as a metric in Table 1, the square-root of Equation (16) was used. To be consistent with shape classification experiments, we chose the 5-layer NTK1 and 9-layer NTK2 to train and evaluate the similarity between two shapes. The detailed analysis for the role of the neural network layers on shape matching is available at Appendix A.5.2. The final outputs from the networks were evaluated with all of the shape similarity measures used in the experiments.

A.1.2 Few-shot shape classification

The ModelNet40-FS dataset [26] was used in the case of evaluating few-shot learning capability of neural varifold kernels (NTK1 and NTK2) with popular few-shot learning methods including Prototypical Net [30], Relation Net [31], PointBERT [32], and PCIA [26]. The ModelNet40-FS dataset [26] consists of 30 training and 10 unseen classes for training the backbone network and evaluating few-shot shape classification. The implementation of the baseline methods and backbone networks is based on [26]. The computation of the neural varifold kernels (NTK1 and NTK2) is based on the *neural tangent* library [33]. In this experiment there are two different versions of NTK1 and NTK2s used. First of all, NTK1 and NTK2 are directly computed from the original point cloud features (i.e., positions and their normals). As few-shot learning is usually based on pre-trained neural networks, NTK1 (DGCNN) and NTK2 (DGCNN) are computed from point-wise feature extracted from the backbone Dynamic graph convolutional neural network (DGCNN). DGCNN [6], used in the experiments, consists of 4 EdgeConv layers [26]. The point-wise features are defined as the concatenation of the convolutional features extracted from all 4 EdgeConv layers of the DGCNN. Furthermore, global features are defined as the max-pooling of the point-wise features.

The evaluation was conducted using the standard few-shot classification setup: N-way K-shot Q-query. In this setup, N-way refers to the number of classes used for training and evaluation; K-shot indicates the number of samples per class used for training; and Q-query specifies the number of samples per class used for evaluating the classification accuracy. All methods are evaluated in two different few-shot learning scenarios: 5way-1shot-15query and 5way-5shot-15query. It is important to note that the reported accuracy in Table 2 represents the average accuracy and its 95% confidence intervals for 700 test cases (i.e., 700 test cases of N-way K-shot 15query).

In addition, we evaluate the scenario when pre-training data/models are not available. In this experimental setup, each method was also trained with a varying number of training samples per class, ranging from 1 to 50, and we evaluated their performance on the full ModelNet10/40 validation datasets. The number of 1024 points and their corresponding normals for each object were sampled from the original meshes of the Princeton ModelNet benchmark [34]. The proposed neural varifold methods are compared with popular neural networks on point clouds including PointNet [7], DGCNN

[6], as well as the kernel method [13]. The computation of the neural varifold kernels (NTK1 and NTK2) is based on the *neural tangent* library [33]. To make the results more consistent, samples were randomly chosen and iterated 20 times with different seeds. Both NTK1 and NTK2 are required to fix the number of layers corresponding to the equivalent finite-width neural networks. NTK1 uses 5 fully connected neural network layers while NTK2 adopts 9 fully connected neural network layers. Each layer consists of MLP, layer normalisation and ReLU activation for both NTK1 and NTK2. The shape classification performance on the full ModelNet data is available at Appendix A.3. The criteria used to choose the number of layers and different layer width for both NTK1 and NTK2 are available at Appendix A.5.

A.1.3 Shape reconstruction

Lastly, for shape reconstruction from point clouds, ShapeNet dataset [35] was used. In particular, we followed the data processing and shape reconstruction experiments from [36], i.e., 20 objects from the individual 13 classes were randomly chosen and used for evaluating the shape reconstruction performance. For each shape, 2048 points were sampled from the surface and used for the reconstruction. Our approach was compared with the state-of-the-art shape reconstruction methods including Neural Splines [36], SIREN [37] and neural kernel surface reconstruction (NKSР) [38]. To be consistent with existing point cloud based shape reconstruction literature, CD and EMD were used to evaluate each method. Unlike CD, EMD has a number of different implementations for solving a sub-optimisation problem about the transportation of mass. In this study, we borrowed the EMD implementation code from [39]. In the experiment, we fixed the number of NTK1 network layers as 1. This is because there is no significant performance change when different number of network layers is used. The shape reconstruction using neural varifold is heavily influenced by the approaches from kernel interpolation [40] and neural splines [36]. The implementation details are available at Appendix A.2. In addition, the shape reconstruction results with different number of points (i.e., 512 and 1024) are available at Appendix A.5.4. The visualisation of the ShapeNet reconstruction performance by all the methods compared is available at Appendix A.6.

A.2 Kernel based shape reconstruction

Consider a set of surface points $\mathcal{X} = \{x_1, \dots, x_k\}$ and their corresponding normals $\mathcal{Z} = \{z_1, \dots, z_k\}$ sampled on an unknown surface \mathcal{M} , i.e., $\mathcal{X} \subset \mathcal{M}$. Using an implicit surface representation, all x in \mathcal{M} satisfy $f(x) = 0$ for some suitable function f . The best way to approximate the function f is to generate off-surface points and to interpolate the zero iso-surface. Given $\mathcal{Y} = \{y_1, \dots, y_k\}, \forall y_i = 0$ and the distance parameter δ , we define $\mathcal{X}_\delta^- = \{x_1 - \delta z_1, \dots, x_k - \delta z_k\}$, $\mathcal{X}_\delta^+ = \{x_1 + \delta z_1, \dots, x_k + \delta z_k\}$, $\mathcal{Y}_\delta^- = \{-\delta, \dots, -\delta\}$, and $\mathcal{Y}_\delta^+ = \{\delta, \dots, \delta\}$ in a similar manner. Taking the set unions $\hat{\mathcal{X}} = \mathcal{X} \cup \mathcal{X}_\delta^- \cup \mathcal{X}_\delta^+$, $\hat{\mathcal{Z}} = \mathcal{Z} \cup \mathcal{Z} \cup \mathcal{Z}$ and $\hat{\mathcal{Y}} = \mathcal{Y} \cup \mathcal{Y}_\delta^- \cup \mathcal{Y}_\delta^+$, the training data tuple $(\mathcal{X}_{\text{train}}, \mathcal{Y}_{\text{train}}) = (\{\hat{\mathcal{X}}, \hat{\mathcal{Z}}\}, \hat{\mathcal{Y}})$ (cf. symbols $\mathcal{X}_{\text{train}}$ and $\mathcal{Y}_{\text{test}}$ are used for multi point clouds) can be used to obtain the *implicit representation of the surface*.

Let us define regular voxel grids $\mathcal{X}_{\text{grid}}$ on which all the extended point clouds $\hat{\mathcal{X}}$ lie. Note that there is no straightforward way to define normal vectors on the regular voxel grids, which are required for PointNet-NTK1 computation. Here, we assign their normals $\mathcal{Z}_{\text{grid}}$ as the unit normal vector to z-axis. Then the signed distance corresponding to the regular grid $\mathcal{X}_{\text{test}} = \{\mathcal{X}_{\text{grid}}, \mathcal{Z}_{\text{grid}}\}$ can be computed by kernel regression with neural splines or PointNet-NTK1 kernels $K(\mathcal{X}_{\text{train}}, \mathcal{X}_{\text{train}})$ and $K(\mathcal{X}_{\text{test}}, \mathcal{X}_{\text{train}})$, i.e.,

$$\mathcal{Y}_{\text{test}} = K(\mathcal{X}_{\text{test}}, \mathcal{X}_{\text{train}})[K(\mathcal{X}_{\text{train}}, \mathcal{X}_{\text{train}}) + \lambda \mathbf{I}]^{-1} \mathcal{Y}_{\text{train}}, \quad (18)$$

where $\mathcal{Y}_{\text{train}}$ and $\mathcal{Y}_{\text{test}}$ are the signed distances for the extended point clouds and the regular grids, respectively. With the marching cube algorithm in [41, 42], the implicit signed distance values on the regular grid with any resolution can be reformulated to the mesh representation.

A.3 Shape classification with the full ModelNet dataset

The overall shape classification accuracy with neural varifold and the comparison with state-of-the-art methods on both ModelNet10 and ModelNet40 are given in Table 5, where the entire training data is used. The table shows that the finite-width neural network based shape classification methods (i.e., PointNet, PointNet++ and DGCNN) in general outperform the kernel based approaches, i.e., CT,

Table 5: ModelNet classification.

Methods	ModelNet10	ModelNet40
PointNet*[1]	94.4	90.5
PointNet++[2]	94.1	91.9
DGCNN [3]	95.0	92.2
CT	89.0	80.5
NTK1	92.2	87.4
NTK2	92.2	86.5

* Point cloud inputs are positions and unit normal vectors – 6-feature vectors; note that the original paper’s reported accuracy for ModelNet40 is 89.2% with only positions forming 3-feature vectors as inputs.

NTK1 and NTK2. DGCNN shows the best accuracy on both ModelNet10 and ModelNet40 amongst the methods compared. In the case of kernel based methods, NTK1 outperforms both NTK2 and CT. The results are largely expected since the infinite-width neural networks with either NTK or NNGP kernel representations underperform in comparison with the equivalent finite-width neural networks [43] when sufficient training samples are available. The computational complexity of kernel-based approaches is quadratic. With the ModelNet10 dataset containing 4899 samples, NTK1 and NTK2 respectively require approximately 12 hours and 6 hours of training time, whereas PointNet and DGCNN achieve similar accuracy with nearly 1 hour of training time using the entire dataset.

Table 6: Shape classification performance of NTK1 and NTK2 with different number of neural network layers adopted in MLP and Conv1D on ModelNet40.

Number of Layers	PointNet-NTK1 (5-sample)	PointNet-NTK2 (5-sample)
1-layer MLP	67.70 ± 1.66	64.70 ± 1.34
3-layer MLP	69.06 ± 1.57	66.79 ± 1.50
5-layer MLP	69.29 ± 1.48	67.34 ± 1.45
7-layer MLP	69.29 ± 1.43	67.64 ± 1.47
9-layer MLP	69.21 ± 1.48	67.81 ± 1.47
1-layer Conv1D	66.06 ± 1.71	63.20 ± 1.30
3-layer Conv1D	68.82 ± 1.62	66.88 ± 1.52
5-layer Conv1D	69.09 ± 1.51	67.42 ± 1.45
7-layer Conv1D	68.87 ± 1.53	67.77 ± 1.41
9-layer Conv1D	68.68 ± 1.46	67.89 ± 1.47

A.4 Pseudo-code for PointNet-NTK Computation and Its Applications in Shape Matching, Classification, and Reconstruction

Algorithm 1 PointNet-NTK Computations

Require: $s_i = \{\{x_1, z_1\}, \dots, \{x_{\hat{m}}, z_{\hat{m}}\}\}$, $s_j = \{\{\hat{x}_1, \hat{z}_1\}, \dots, \{\hat{x}_{\hat{m}}, \hat{z}_{\hat{m}}\}\}$, $N > 0$

if PointNet-NTK1 **then**

- $\mathbf{X}, \hat{\mathbf{X}} \leftarrow \{x_1, x_2, \dots, x_{\hat{m}}\}, \{\hat{x}_1, \hat{x}_2, \dots, \hat{x}_{\hat{m}}\}$
- $\mathbf{Z}, \hat{\mathbf{Z}} \leftarrow \{z_1, z_2, \dots, z_{\hat{m}}\}, \{\hat{z}_1, \hat{z}_2, \dots, \hat{z}_{\hat{m}}\}$
- $\Theta^{\text{pos}} \leftarrow \text{Algorithm 2 } (\mathbf{X}, \hat{\mathbf{X}}, N)$
- $\Theta^{\text{nor}} \leftarrow \text{Algorithm 2 } (\mathbf{Z}, \hat{\mathbf{Z}}, N)$
- $\Theta^{\text{varifold}} \leftarrow \Theta^{\text{pos}} \odot \Theta^{\text{nor}}$

else if PointNet-NTK2 **then**

- $\mathbf{P} \leftarrow \{\text{CONCAT}(x_1, z_1), \dots, \text{CONCAT}(x_{\hat{m}}, z_{\hat{m}})\}$
- $\hat{\mathbf{P}} \leftarrow \{\text{CONCAT}(\hat{x}_1, \hat{z}_1), \dots, \text{CONCAT}(\hat{x}_{\hat{m}}, \hat{z}_{\hat{m}})\}$
- $\Theta^{\text{varifold}} \leftarrow \text{Algorithm 2 } (\mathbf{P}, \hat{\mathbf{P}}, N)$

end if

return Θ^{varifold}

Remark: As an example, $\mathbf{X} \in \mathbb{R}^{\hat{m} \times 3}$ is formed by concatenating all $x_i \in \{x_1, x_2, \dots, x_{\hat{m}}\}$.

Algorithm 2 NTK Corresponding to N -layer Infinite-width MLP with ReLU Activation*

Require: $\mathbf{X}, \hat{\mathbf{X}}, N > 0$

Initialise $\Theta^{(0)} = \Sigma^{(0)} = \mathbf{X} \hat{\mathbf{X}}^\top$, $\mathbf{d}_\mathbf{X}^{(0)} = (d_1^{(0)}, d_2^{(0)}, \dots) = \text{diag}(\mathbf{X} \mathbf{X}^\top)$,
 $\hat{\mathbf{d}}_{\hat{\mathbf{X}}}^{(0)} = (\hat{d}_1^{(0)}, \hat{d}_2^{(0)}, \dots) = \text{diag}(\hat{\mathbf{X}} \hat{\mathbf{X}}^\top)$

for $h \leftarrow 1$ to N **do**

$\omega_{\hat{i}, \hat{j}}^{(h-1)} \leftarrow \Sigma_{\hat{i}, \hat{j}}^{(h-1)} / \sqrt{d_{\hat{i}}^{(h-1)} \hat{d}_{\hat{j}}^{(h-1)}}, \hat{i}, \hat{j} = 1, 2, \dots, \text{length}(\mathbf{d}_\mathbf{X}^{(h-1)})$

$\dot{\Sigma}^{(h-1)} \leftarrow \mathbf{F}_0(\Sigma^{(h-1)}, \mathbf{d}_\mathbf{X}^{(h-1)}, \hat{\mathbf{d}}_{\hat{\mathbf{X}}}^{(h-1)})$, where $(\mathbf{F}_0)_{\hat{i}, \hat{j}} = 1 - \frac{1}{\pi} \arccos \omega_{\hat{i}, \hat{j}}^{(h-1)}$

$\Sigma^{(h)} \leftarrow \mathbf{F}_1(\Sigma^{(h-1)}, \mathbf{d}_\mathbf{X}^{(h-1)}, \hat{\mathbf{d}}_{\hat{\mathbf{X}}}^{(h-1)})$, where
 $(\mathbf{F}_1)_{\hat{i}, \hat{j}} = \frac{1}{2\pi} \sqrt{d_{\hat{i}}^{(h-1)} \hat{d}_{\hat{j}}^{(h-1)}} (\sqrt{1 - (\omega_{\hat{i}, \hat{j}}^{(h-1)})^2} + (\pi - \arccos \omega_{\hat{i}, \hat{j}}^{(h-1)}) \omega_{\hat{i}, \hat{j}}^{(h-1)})$

$\Theta^{(h)} \leftarrow \Sigma^{(h)} + \Theta^{(h-1)} \dot{\Sigma}^{(h-1)}$

$d_\mathbf{X}^{(h)}, \hat{d}_{\hat{\mathbf{X}}}^{(h)} \leftarrow \frac{1}{2} \mathbf{d}_\mathbf{X}^{(h-1)}, \frac{1}{2} \hat{\mathbf{d}}_{\hat{\mathbf{X}}}^{(h-1)}$

end for

return $\Theta^{(h)}$

* Although **Algorithm 2** assumes the NTK representation corresponding to N -layer MLP with ReLU activation [44, 45, 33], several popular neural network layers have their corresponding closed-form NTK representations [33, 43, 46].

Algorithm 3 Shape Matching

Require: $f(\cdot; \theta), \mathcal{S}, \mathcal{T}, n_{\max} > 0, n_{\text{iter}} = 0$

while $n_{\max} > n_{\text{iter}}$ **do**

$v_{\mathcal{S}} \in \mathbb{R}^{|\mathcal{S}| \times 3}$ vertices of \mathcal{S}

$d_{\mathcal{S}} \leftarrow f(v_{\mathcal{S}}; \theta)$ displacements between \mathcal{S} and \mathcal{T}

$\hat{\mathcal{S}} \leftarrow$ new source shape with deformed vertices $v_{\mathcal{S}} + d_{\mathcal{S}}$

$x_{\hat{\mathcal{S}}}, z_{\hat{\mathcal{S}}} \leftarrow$ sample surface points and corresponding normals from $\hat{\mathcal{S}}$

$x_{\mathcal{T}}, z_{\mathcal{T}} \leftarrow$ sample surface points and corresponding normals from \mathcal{T}

$\hat{s}_{\hat{\mathcal{S}}} \leftarrow \{x_{\hat{\mathcal{S}}}, z_{\hat{\mathcal{S}}}\}$

$\hat{s}_{\mathcal{T}} \leftarrow \{x_{\mathcal{T}}, z_{\mathcal{T}}\}$

Compute $\|s_{\hat{\mathcal{S}}} - s_{\mathcal{T}}\|_{\text{varifold}}^2$ in Equation (16) using **Algorithm 1**

Backpropagate and update θ

$\mathcal{S} \leftarrow \hat{\mathcal{S}}$

$n_{\text{iter}} \leftarrow n_{\text{iter}} + 1$

end while

Remark: Here $f(\cdot; \theta)$ is a 2-layer MLP neural network, θ is the weights of the neural network f . \mathcal{S} and \mathcal{T} are the source and target shapes, respectively.

Algorithm 4 Shape Classification

Require: $\mathcal{X}_{\text{train}} = \{s_1, s_2, \dots, s_l\}, \mathcal{Y}_{\text{train}} = \{y_1, y_2, \dots, y_l\}, \mathcal{X}_{\text{test}} = \{s_{l+1}, s_{l+2}, \dots, s_{\hat{n}}\}, N > 0$, where $s_i = \{p_1, p_2, \dots, p_{\hat{m}}\}, i = 1, 2, \dots, \hat{n}$

for $i \leftarrow 1$ to l **do**

for $j \leftarrow 1$ to l **do**

$\Theta^{\text{varifold}}(s_i, s_j) \leftarrow \text{Algorithm 1}(s_i, s_j, N)$

Aggregate points $\Theta_{\text{train}_{(i,j)}}^{\text{varifold}} \leftarrow \sum_{\hat{i} \leq \hat{m}} \sum_{\hat{j} \leq \hat{m}} \Theta^{\text{varifold}}(p_i \in s_i, p_j \in s_j)$

end for

end for

for $i \leftarrow l + 1$ to \hat{n} **do**

for $j \leftarrow l + 1$ to \hat{n} **do**

$\Theta^{\text{varifold}}(s_i, s_j) \leftarrow \text{Algorithm 1}(s_i, s_j, N)$

Aggregate points $\Theta_{\text{test}_{(i,j)}}^{\text{varifold}} \leftarrow \sum_{\hat{i} \leq \hat{m}} \sum_{\hat{j} \leq \hat{m}} \Theta^{\text{varifold}}(p_i \in s_i, p_j \in s_j)$

end for

end for

end for

$\mathcal{Y}_{\text{test}}^{\text{pred}} \leftarrow \Theta_{\text{test}}^{\text{varifold}}(\mathcal{X}_{\text{test}}, \mathcal{X}_{\text{train}})(\Theta_{\text{train}}^{\text{varifold}}(\mathcal{X}_{\text{train}}, \mathcal{X}_{\text{train}}) + \lambda I)^{-1} \mathcal{Y}_{\text{train}}$

Algorithm 5 Shape Reconstruction[†]

Require: $\mathcal{X} = \{x_1, \dots, x_k\}$, $\mathcal{Z} = \{z_1, \dots, z_k\}$, $\mathcal{Y} = \{y_1, \dots, y_k\}$, δ , $\mathcal{X}_{\text{grid}}$, $\mathcal{Z}_{\text{grid}}$, $N > 0$

Ensure: $\forall y_i = 0$ and $\delta > 0$

$$\begin{aligned} \mathcal{X}_\delta^-, \mathcal{X}_\delta^+ &\leftarrow \{x_1 - \delta z_1, \dots, x_k - \delta z_k\}, \{x_1 + \delta z_1, \dots, x_k + \delta z_k\} \\ \mathcal{Y}_\delta^-, \mathcal{Y}_\delta^+ &\leftarrow \{-\delta, \dots, -\delta\}, \{\delta, \dots, \delta\} \\ \hat{\mathcal{X}}, \hat{\mathcal{Z}}, \hat{\mathcal{Y}} &\leftarrow \mathcal{X} \cup \mathcal{X}_\delta^- \cup \mathcal{X}_\delta^+, \mathcal{Z} \cup \mathcal{Z} \cup \mathcal{Z}, \mathcal{Y} \cup \mathcal{Y}_\delta^- \cup \mathcal{Y}_\delta^+ \\ \mathcal{X}_{\text{train}}, \mathcal{Y}_{\text{train}} &\leftarrow \{\hat{\mathcal{X}}, \hat{\mathcal{Z}}\}, \hat{\mathcal{Y}} \\ \Theta^{\text{varifold}}(\mathcal{X}_{\text{train}}, \mathcal{X}_{\text{train}}) &\leftarrow \text{Algorithm 1}(\mathcal{X}_{\text{train}}, \mathcal{X}_{\text{train}}, N) \\ \mathcal{X}_{\text{test}} &\leftarrow \{\mathcal{X}_{\text{grid}}, \mathcal{Z}_{\text{grid}}\} \\ \Theta^{\text{varifold}}(\mathcal{X}_{\text{test}}, \mathcal{X}_{\text{train}}) &\leftarrow \text{Algorithm 1}(\mathcal{X}_{\text{test}}, \mathcal{X}_{\text{train}}, N) \\ \mathcal{Y}_{\text{test}}^{\text{pred}} &= \Theta^{\text{varifold}}(\mathcal{X}_{\text{test}}, \mathcal{X}_{\text{train}})[\Theta^{\text{varifold}}(\mathcal{X}_{\text{train}}, \mathcal{X}_{\text{train}}) + \lambda I]^{-1} \mathcal{Y}_{\text{train}} \\ \mathcal{S}_{\text{recon}} &\leftarrow \text{Marching cube algorithm [42]}(\mathcal{X}_{\text{test}}, \mathcal{Y}_{\text{test}}^{\text{pred}}) \end{aligned}$$

[†]Please refer to a more detailed explanation of terms and equations in Appendix A.2.

A.5 Ablation analysis

A.5.1 Neural varifolds with different number of neural network layers

This section shows the shape classification results based on different number of neural network layers. In this experiment, we randomly choose 5 samples per class on the training set of ModelNet40 and evaluate on its validation set. As shown in Section 4, we iterate the experiments 20 times with different random seeds. The key concept of the PointNet [7] is the permutation invariant convolution operations on point clouds. For example, MLP or Conv1D with 1 width convolution window is permutation invariance. In this experiment, we choose different number of either MLP or Conv1D layers, and check how it performs on the ModelNet40 dataset. As shown in Table 6, the classification accuracy of NTK1 with Conv1D operation is lower in comparison with the ones with MLP layers. In particular, 5-layer and 7-layer MLPs show similar performance with the NTK1 architecture, i.e., 69.29% classification accuracy. In order to reduce the computational cost, we recommend fixing the number of layers in NTK1 to 5. In the case of NTK2, its performance increases as more layers are being added for it with both MLP and Conv1D operations. Furthermore, NTK2 with Conv1D operation shows slightly higher classification accuracy in comparison with the ones with MLP layers. The percentage of the performance improvement becomes lower as the number of layers increases. In particular, 9-layer MLP versus 7-layer MLP for NTK2 only brings 0.2% improvement; therefore, it is computationally inefficient to increase the number of layers anymore. Although NTK2 with 9-layer Conv1D achieves 0.08% higher accuracy than the one with 9-layer MLP, NTK2 with 9-layer MLP rather than Conv1D is used for the rest of the experiments in order to make the architecture consistent with the NTK1.

A.5.2 Shape matching with different number of neural network layers

Table 7: Ablation analysis for shape matching with respect to different number of neural network layers within NTK psueo-metrics. The number inside of the brackets (·) indicates the number of layers used for computing the NTK pseudo-metrics.

Metric	NTK1 (1)	NTK1 (5)	NTK1 (9)
CD	2.82E-1	2.67E-1	2.99E-1
EMD	2.43E5	2.09E5	2.46E5
CT	2.19E3	2.17E3	2.17E3
NTK1	7.74E3	4.93E3	4.90E3
NTK2	2.56E3	1.54E3	1.92E3

Metric	NTK2 (1)	NTK2 (5)	NTK2 (9)
CD	2.59E-1	2.61E-1	2.64E-1
EMD	2.14E5	2.32E5	1.93E5
CT	2.15E3	2.17E3	2.15E3
NTK1	9.57E3	8.70E3	9.98E3
NTK2	1.28E3	1.41E3	1.53E3

In this section, the behavior of the NTK pseudo-metrics with respect to different number of layers is evaluated. Note that the neural network width is not considered in this scenario as all pseudo-metrics are computed analytically (i.e., infinite-width). In this study, simple shape matching networks were trained solely by NTK psuedo-metrics with different number of layers. Table 7 shows that the shape matching network trained with the 5-layer NTK1 metric achieves the best score with respect to CD, EMD, CT and NTK2 metrics, while the one with the 9-layer NTK1 metric achieves the best score with respect to CT and NTK1 metrics. This is in accordance with the ablation analysis for shape classification, where 5-layer NTK1 achieves the best classification accuracy in the ModelNet10 dataset. In comparison, NTK2 shows a mixed signal. The shape matching network trained with the 1-layer NTK2 metric achieves the best outcome with respect to Chamfer, CT and NTK2 metrics, while the one trained with the 9-layer NTK2 achieves the best results with respect to EMD and CT metrics. The network trained with 5-layer NTK2 shows the best result with respect to the NTK1 metric. This is not exactly in accordance with respect to shape classification with the NTK2 metric, where the shape classification accuracy improves as the number of layers increases. However, training a neural network always involves some non-deterministic nature; therefore, it is yet difficult to conclude whether the number of neural network layers is important for improving the shape matching quality or not.

A.5.3 Shape classification with different neural network width

In this section, we analyse how the neural network width can impact on shape classification using the 9-layer MLP-based NTK2 by varying the width settings from 128, 512, 1024 and 2048 to infinite-width configurations. We trained the model on 5 randomly sampled point clouds per class from the ModelNet10 training set. The evaluation was carried out on the ModelNet10 validation set. This process was repeated five times with different random seeds, and the average shape classification accuracy was computed. Notably, NTK1 was excluded from this experiment due to the absence of a finite-width neural network layer corresponding to the elementwise product between two neural tangent kernels of infinite-width neural networks. The results presented in Table 8 demonstrate that the analytical NTK (infinite-width NTK) outperforms the empirical NTK computed from the corresponding finite-width neural network with a fixed width size. Furthermore, computing empirical NTK with respect to different length of parameters is known to be expensive as the empirical NTK is expressed as the outer product of the Jacobians of the output of the neural network with respect to the parameters. The details of the computational complexity and potential acceleration have been studied in [47]. However, if the finite-width neural networks are trained with the standard way instead of using empirical NTKs on a large dataset (e.g., CIFAR-10), then finite-wdith neural networks can outperform the neural tangent regime with performance significant margins [43, 24]. In other words, there is still a large gap understanding regarding training dynamics between the finite-width neural networks and their empirical neural kernel representations.

Table 8: Shape classification performance of 9-layer NTK2 with different neural network width.

Width for each layer	NTK2 (5-sample)
128-width	78.74 ± 3.30
512-width	80.08 ± 3.02
1024-width	79.97 ± 3.24
2048-width	80.46 ± 3.13
infinite-width	81.74 ± 3.16

A.5.4 Shape reconstruction with different point cloud sizes

In this section, we compare shape reconstruction results with different point cloud sizes, i.e., 512, 1024 and 2048 points. As indicated in Tables 4, 9 and 10, NTK1 and neural splines show that the quality of the reconstructions is degraded as the number of points decreases. For NKS, its reconstruction quality becomes worse as the number of point clouds decreases for most categories, but few categories (i.e., cabinet and vessel) show the opposite trend. In the case of SIREN, the convergence of the SIREN network plays more important role for the shape reconstruction quality. For example, the shape reconstruction results by SIREN on the airplane category show that the shape reconstruction with 1024 points is better than that with 2048 points. This is due to the non-deterministic nature of DNN libraries, i.e., it is difficult to control the convergence of the SIREN

Table 9: ShapeNet 3D mesh reconstruction with 1024 points (mean/median values $\times 10^3$).

Metric	Method	Airplane	Bench	Cabinet	Car	Chair	Display	Lamp	Speaker	Rifle	Sofa	Table	Phone	Vessel
CD (mean)	SIREN	0.936	1.499	3.134	5.363	2.492	3.635	2.536	4.109	2.134	3.660	2.264	1.674	1.339
	Neural Splines	11.640	1.905	2.264	2.440	2.983	4.770	1.418	3.437	0.439	1.924	3.936	9.026	2.255
	NKSR	1.898	3.506	6.224	2.286	3.584	46.997	9.229	4.138	0.665	2.029	3.213	2.243	1.285
	PointNet-NTK1	1.584	1.742	2.274	2.494	2.655	5.337	1.465	3.947	0.456	1.870	2.029	12.138	1.341
CD (median)	SIREN	0.756	1.272	2.466	2.305	1.281	1.385	1.156	3.411	0.487	1.706	1.601	1.390	1.040
	Neural Splines	8.171	1.562	1.830	2.058	2.152	1.548	0.698	3.071	0.359	1.657	1.715	1.594	0.879
	NKSR	1.900	2.245	1.799	2.190	2.116	1.880	2.347	3.488	0.407	1.697	1.695	1.345	0.956
	PointNet-NTK1	0.820	1.701	1.933	1.995	1.522	1.719	0.733	3.045	0.366	1.719	1.643	1.658	1.016
EMD (mean)	SIREN	2.183	3.679	6.385	10.712	5.932	7.527	12.850	8.714	3.164	7.633	4.992	3.645	3.265
	Neural Splines	60.566	6.540	5.338	5.380	15.935	8.882	22.745	6.457	1.878	4.335	11.733	18.019	6.367
	NKSR	12.939	11.990	16.684	7.571	21.706	44.190	32.236	12.486	3.613	4.930	14.917	6.609	6.715
	PointNet-NTK1	6.704	5.984	5.301	5.907	14.868	11.507	29.595	8.070	1.773	4.596	11.606	24.903	3.841
EMD (median)	SIREN	1.982	3.211	5.232	4.699	5.678	3.567	2.916	5.548	1.351	3.804	3.122	3.415	2.552
	Neural Splines	35.458	4.713	4.745	4.779	11.570	3.915	5.719	4.575	1.334	3.650	5.041	4.828	2.276
	NKSR	11.317	6.933	5.035	5.432	9.807	8.597	7.871	8.397	1.765	3.524	8.140	3.400	2.354
	PointNet-NTK1	3.716	4.659	5.050	4.598	7.613	4.062	9.168	5.456	1.364	4.105	4.257	4.710	2.209

 Table 10: ShapeNet 3D mesh reconstruction with 512 points (mean/median values $\times 10^3$).

Metric	Method	Airplane	Bench	Cabinet	Car	Chair	Display	Lamp	Speaker	Rifle	Sofa	Table	Phone	Vessel
CD (mean)	SIREN	1.385	1.992	14.975	4.323	2.813	3.094	7.874	5.426	3.731	3.582	10.423	2.524	2.278
	Neural Splines	21.410	3.752	2.818	2.985	5.217	5.089	2.050	4.393	0.565	2.228	5.953	8.721	2.699
	NKSR	3.974	6.265	3.545	2.594	5.348	NA	9.859	5.259	17.419	2.059	6.636	1.677	1.540
	PointNet-NTK1	2.454	2.674	2.565	3.233	3.793	6.087	2.193	4.045	0.550	2.252	2.702	14.349	2.090
CD (median)	SIREN	0.715	1.678	3.635	3.122	1.914	1.672	1.540	4.707	1.156	2.256	1.746	1.497	1.130
	Neural Splines	21.040	2.466	1.935	2.369	3.347	2.058	1.023	3.361	0.385	1.918	2.411	1.717	1.226
	NKSR	2.627	3.336	1.894	2.015	3.752	NA	4.427	3.753	0.906	1.833	3.555	1.411	0.856
	PointNet-NTK1	1.243	2.246	2.106	2.316	2.473	1.968	1.346	3.330	0.387	1.890	1.963	2.013	1.309
EMD (mean)	SIREN	3.411	5.833	24.404	9.460	7.366	6.558	26.828	13.584	5.224	6.457	16.578	4.764	4.831
	Neural Splines	120.415	11.749	7.478	6.057	26.382	11.486	30.216	8.686	3.048	5.128	25.433	19.087	8.431
	NKSR	24.959	21.190	11.433	9.346	30.485	NA	36.050	18.147	13.115	5.226	24.257	4.701	8.605
	PointNet-NTK1	13.826	9.217	5.614	11.548	16.465	13.501	35.540	8.334	2.436	6.010	15.663	27.025	5.897
EMD (median)	SIREN	1.964	5.036	8.656	6.643	5.553	3.650	14.281	14.499	2.296	4.682	3.735	3.779	3.012
	Neural Splines	115.527	9.698	4.679	4.863	20.006	4.476	10.834	5.405	1.548	4.234	8.205	4.742	3.147
	NKSR	25.234	14.795	4.405	6.669	16.082	NA	10.727	8.655	3.132	4.147	9.839	3.595	2.650
	PointNet-NTK1	9.863	6.122	4.758	7.171	6.822	5.076	9.296	5.683	1.626	4.497	7.455	6.658	3.313

NA indicates that the method fails to reconstruct few shapes in the given class.

A.6 Visualisation of ShapeNet reconstruction results

In this section, we present additional visualisations of shape reconstruction outcomes obtained through three baseline methods (i.e., SIREN, neural splines, and NKSR), along with the proposed NTK1 method, across 13 categories of ShapeNet benchmarks. Five shape reconstruction results are illustrated for each category. Specifically, Figure 3 showcases examples from the Airplane, Bench, and Cabinet categories. Figure 4 exhibits five instances of shape reconstruction outcomes for the Car, Chair, and Display categories. Moving on to Figure 5, it displays examples from the Lamp, Speaker, and Rifle categories. Similarly, Figure 6 demonstrates five instances of shape reconstruction results for the Sofa, Table, and Phone categories. Finally, Figure 7 focuses on the shape reconstruction results for the Vessel category.

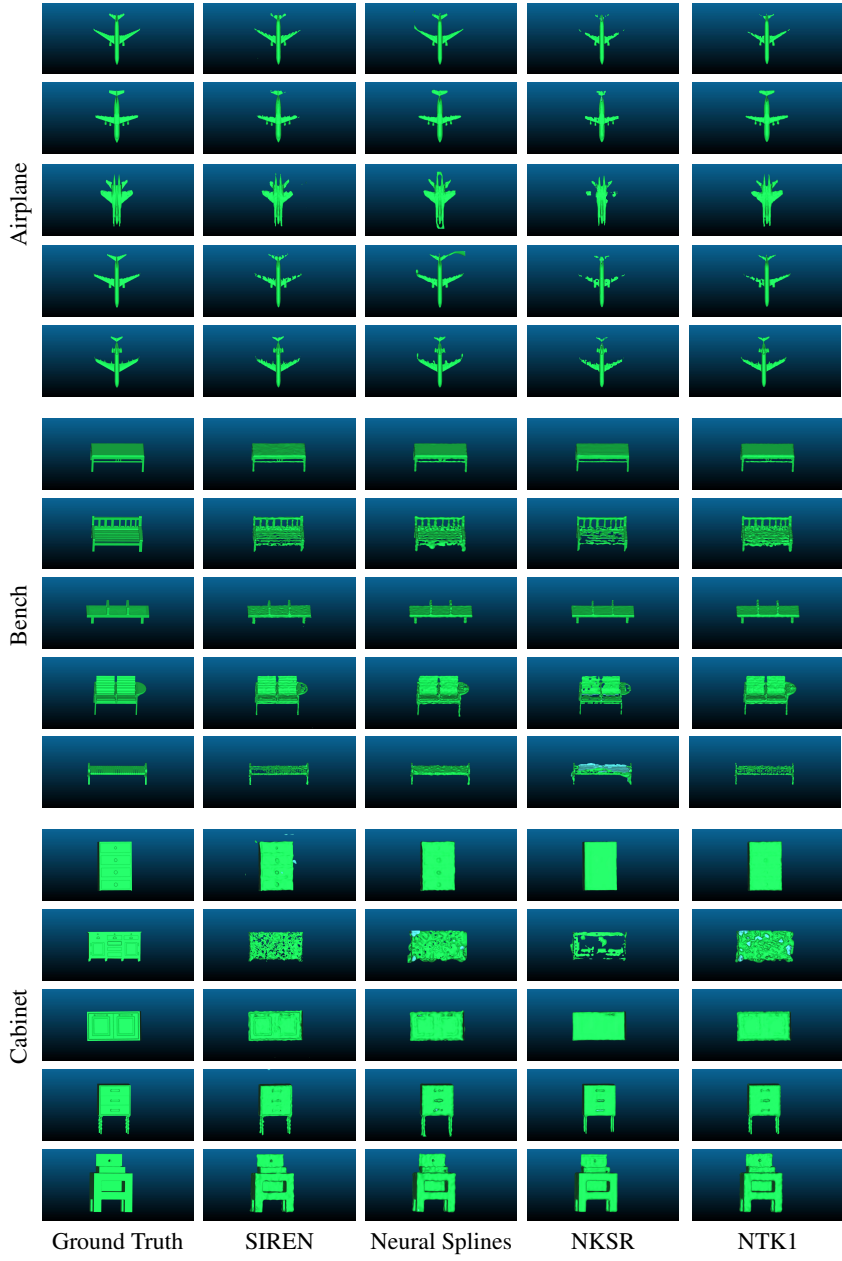


Figure 3: Visualisation of shape reconstruction results from SIREN, Neural Splines, NKS1 and NTK1 for the Airplane, Bench and Cabinet categories.

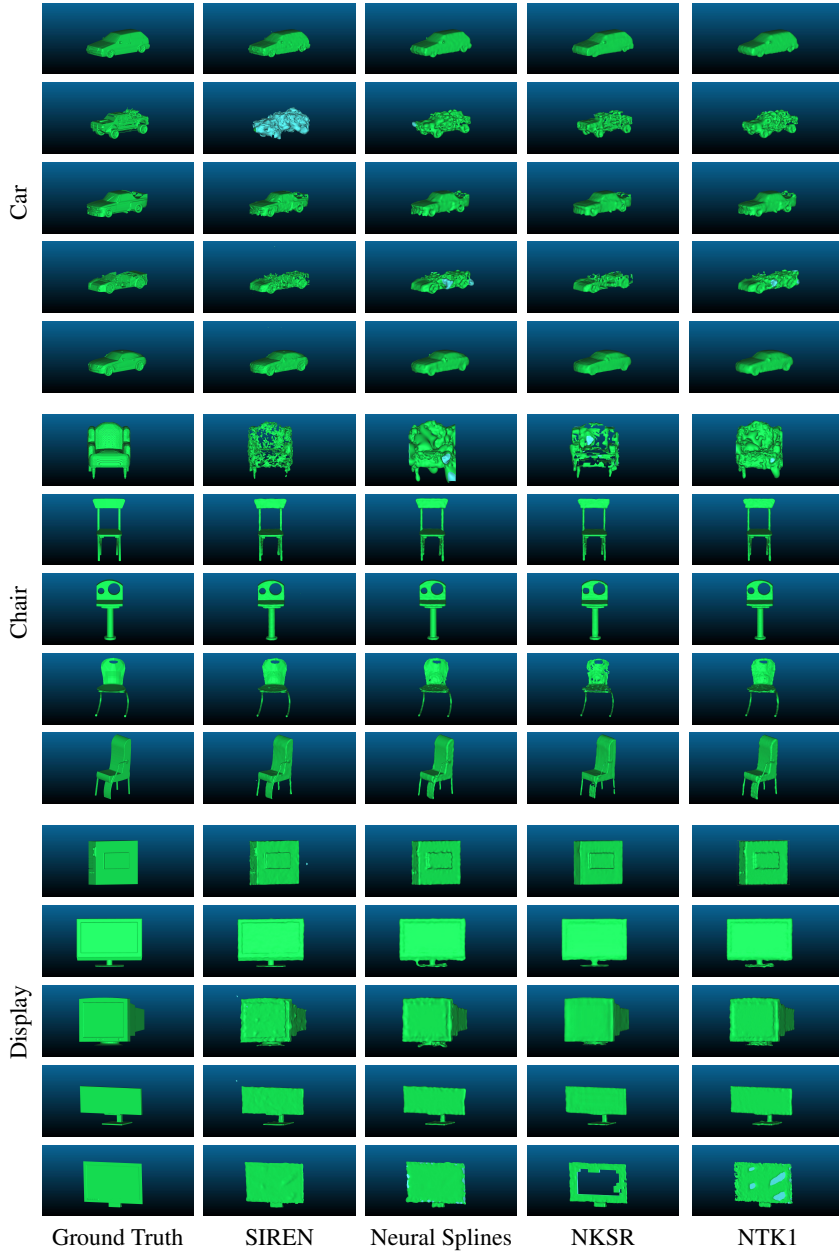


Figure 4: Visualisation of shape reconstruction results from SIREN, Neural Splines, NKSR and NTK1 for the Car, Chair and Display categories.



Figure 5: Visualisation of shape reconstruction results from SIREN, Neural Splines, NKSR and NTK1 for the Lamp, Speaker and Rifle categories.



Figure 6: Visualisation of shape reconstruction results from SIREN, Neural Splines, NKS and NTK1 for the Sofa, Table and Phone categories.

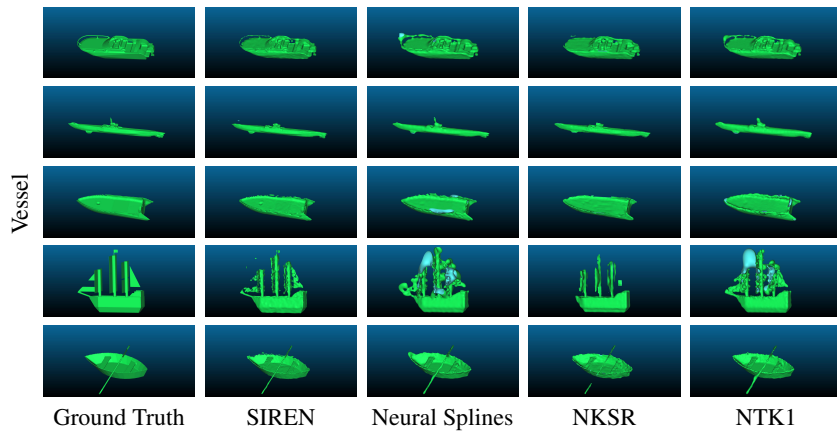


Figure 7: Visualisation of shape reconstruction results from SIREN, Neural Splines, NKSR and NTK1 for the Vessel category.